

Ultrafast Electron Diffraction: Oriented Molecular Structures in Space and Time

J. Spencer Baskin and Ahmed H. Zewail*^[a]

The technique of ultrafast electron diffraction allows direct measurement of changes which occur in the molecular structures of isolated molecules upon excitation by femtosecond laser pulses. The vectorial nature of the molecule–radiation interaction also ensures that the orientation of the transient populations created by the laser excitation is not isotropic. Here, we examine the influence on electron diffraction measurements—on the femtosecond and picosecond timescales—of this induced initial anisotropy and subsequent inertial (collision-free) molecular reorientation, accounting for the geometry and dynamics of a laser-induced reaction (dissociation). The orientations of both the residual ground-state population and the excited- or product-state populations evolve in time, with different characteristic rotational de-

phasing and recurrence times due to differing moments of inertia. This purely orientational evolution imposes a corresponding evolution on the electron scattering pattern, which we show may be similar to evolution due to intrinsic structural changes in the molecule, and thus potentially subject to misinterpretation. The contribution of each internuclear separation is shown to depend on its orientation in the molecular frame relative to the transition dipole for the photoexcitation; thus not only bond lengths, but also bond angles leave a characteristic imprint on the diffraction. Of particular note is the fact that the influence of anisotropy persists at all times, producing distinct differences between the asymptotic “static” diffraction image and the predictions of isotropic diffraction theory.

1. Introduction

Standard gas-phase electron diffraction is a powerful technique for the study of molecular structure, through the simple concept of interference between the electron scattering from each pair of atomic nuclei in the molecule. Thousands of molecular structures have been determined by this technique over the past seventy years.^[1] Scattering from a typical thermal gas sample, in which molecules are randomly located and randomly oriented, is axially symmetric about the incident electron beam, with the interference contributions yielding circular diffraction rings (albeit on an intense incoherent atomic scattering background) in the intensity pattern detected on a screen placed beyond the sample. Oscillation frequencies in the radial intensity pattern reflect the distribution of intramolecular atomic separation distances, and in the ideal case, extraction of the internuclear separations by Fourier analysis allows the three-dimensional structure of the molecule to be deduced.

Over the last ten years, ultrafast electron diffraction (UED) has been developed for the purpose of using electron diffraction as a direct probe of the molecular structure of isolated molecules as they evolve after excitation by a femtosecond laser pulse. With this technique, the rise and decay of structurally distinct populations—resulting, for example, from dissociation or isomerization of the sample of excited molecules—can be observed in real time, and the structures of intermediate states with lifetimes as short as picoseconds can be directly determined. Overviews of the work of the Caltech group in this field, which has provided unique insights into numerous molecular systems, have recently been published.^[2,3]

From the beginning of UED, it has been recognized that the vectorial nature of the molecule–radiation interaction imposes

an orientational anisotropy on the transient populations created by the laser excitation.^[4] Specifically, the distribution of molecular transition-dipole-moment vectors of excited molecules at the instant of excitation is determined by a cosine-squared dependence of the absorption strength on the angle between each such vector and the laser polarization vector of a linearly polarized laser pulse. Theoretical calculations of electron diffraction scattering patterns for samples frozen at this initial configuration have been presented for a variety of assumptions for linear^[4,5] as well as nonlinear^[4] molecules, demonstrating pronounced deviations from isotropic theory. In gas-phase, collisionless samples, this initial anisotropy will decay due to rotation of the individual molecules of the sample on a time-scale dictated by the molecular moments of inertia, the direction of the transition dipole in the molecular frame, and the sample rotational temperature, and this timescale has been within the time resolution of several picoseconds employed for many of the already completed UED studies. For this reason, and because the anisotropy which remains after the initial decay is typically much smaller than the starting value, isotropic theory has been applied successfully in fitting experimental results to date.

However, as UED has matured, the importance of understanding more completely the nature of orientation effects has

[a] J. S. Baskin, Prof. A. H. Zewail
Laboratory for Molecular Sciences
Arthur Amos Noyes Laboratory of Chemical Physics
California Institute of Technology, Pasadena CA 91125 (USA).
Fax: (+1) 626-792-8456
E-mail: zewail@caltech.edu

remained clear. Improvements in signal-to-noise and time resolution have made the investigation of *time-dependent* orientation on diffraction even more essential, especially so in studies of cold or large (and thus slowly rotating) molecules, for which the initial, highly aligned population distributions would persist on picosecond and longer timescales. A formal theoretical treatment, using density matrices, of time-dependent orientation in UED has been published, specialized to a bound diatomic molecule.^[6] For this limited case, the focus was on vibrational and rotational coherences without development of the consequences.

Here we develop the theory of the influence of time-dependent orientation on electron diffraction measurements, on the femtosecond and picosecond timescales, and illustrate the consequences within the context of UED studies of chemical reactions. For this purpose, we incorporate the theory of reorientation dynamics for prompt dissociation reactions, as developed previously,^[7,8] assuming inertial (collision-free) symmetric-top rotation and accounting for the anisotropic distributions of the angular momentum of dissociation products, and connect it with the orientation-dependent diffraction for static anisotropy.^[4] Examples are presented to illustrate clearly the consequences of the evolving anisotropy of both the ground- and product-state populations at all times.

2. Theory

2.1. The Role of Molecular Orientation in UED

A schematic representation of the UED experiment is given in Figure 1. Within a vacuum chamber, packets of electrons of wavelength λ and wave vector \mathbf{k}_0 ($k_0 = \frac{2\pi}{\lambda}$) are directed at a stream of gas-phase molecules emanating from a molecular beam, and the resulting pattern of scattered electron intensity is collected in the far field by a planar detector. An isotropic gas sample will produce electron scattering that is cylindrically symmetric about \mathbf{k}_0 , as illustrated in the Figure. Each direction of elastic scattering is associated with a particular wave vector \mathbf{k} , also of magnitude $\frac{2\pi}{\lambda}$, and a momentum transfer vector $\mathbf{s} = \mathbf{k}_0 - \mathbf{k}$ with magnitude $s = \frac{4\pi}{\lambda} \sin(\theta/2)$, where θ is the angle between \mathbf{k} and \mathbf{k}_0 . The geometric phase shift at the detector in the direction of \mathbf{k} between the electron waves scattered from two atoms, atom i and atom l , is $\mathbf{s} \cdot \mathbf{r}_{il}$, where \mathbf{r}_{il} is the internuclear separation vector of the atomic pair.

Also crossing the scattering volume is a beam of femtosecond laser pulses characterized by the linear polarization ϵ , and the delay between the times of passage of a laser pulse and an electron pulse is precisely determined and adjustable. At the instant that the light pulse crossed the sample, referred to as $t=0$, a fraction of those molecules having transition dipoles favorably oriented with respect to the direction of ϵ will be promoted to an excited state, creating an anisotropic sample (see Figure 1, inset). (It is perhaps useful to note here that, in technical usage, distributions of laser-excited and unexcited ensembles, with axial symmetry about ϵ and a plane of symmetry normal to ϵ ($D_{\infty h}$ point group), are "aligned" rather than "oriented", the latter designation being reserved for distribu-

tions lacking the symmetry plane.^[9] Our use of "orientation" herein, in reference to any vector or set of vectors, should thus be understood in its broad sense as simply referring to the angular aspect of position.) After $t=0$, the sample anisotropy will evolve in a manner determined by the free and independent rotation of both the ground-state and excited-state molecules. In the remainder of this section, we examine the effect on electron scattering of this evolving anisotropy.

Following the notation of Williamson and Zewail (WZ),^[4] the general expression for the molecular scattering intensity term in electron diffraction from a sample of molecules with N atoms is given by Equation (1):

$$I_M(t; \mathbf{s}) = C \sum_{i=1}^N \sum_{\substack{l=1 \\ l \neq i}}^N |f_i(\mathbf{s})| |f_l(\mathbf{s})| \operatorname{Re} \left[e^{i(\eta_i(\mathbf{s}) - \eta_l(\mathbf{s}))} \langle \langle e^{i\mathbf{s} \cdot \mathbf{r}_{il}(t)} \rangle \rangle_{\text{Vib, Rot}} \right] \quad (1)$$

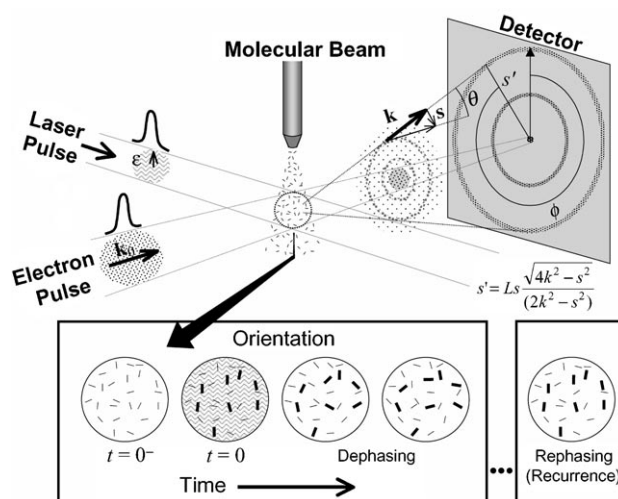


Figure 1. Schematic of the apparatus for ultrafast gas-phase electron diffraction (UED). A linearly polarized laser pulse excites a gas-phase molecular sample in a vacuum chamber, and the sample is probed by a time-delayed electron pulse, with the crossing angle of electron beam and laser beam near 90° . The electron pulse approaching the sample is represented as a tight packet of electrons with a longitudinal extent equal to $v\Delta t$ where v is the electron velocity and Δt is the pulse width. Upon leaving the sample volume, the pulse consists of a core of unscattered electrons surrounded by an expanding cloud of scattered electrons, with intensity variations illustrated schematically by the ring structure shown in the Figure. The electron diffraction pattern is recorded in the far field for a small range of scattering angles by a planar detector centered on the unscattered electron beam path. Each point on the detector is characterized by a particular value of scattering angle θ and azimuthal angle ϕ , to which correspond a unique electron wave vector \mathbf{k} and momentum-transfer vector \mathbf{s} . The radial distance between the detection point and the unscattered beam spot, labeled s' , is given in the Figure in terms of s , k , and camera length L , the distance from the sample volume to the detector along the unscattered beam. Inset: A schematic time series of snapshots of transition dipoles of a molecular gas sample in the interaction volume of the UED apparatus. At $t=0$, the laser pulse with vertical polarization crosses the volume, creating an excited population consisting of molecules with transition dipoles preferentially aligned in the vertical direction (dark lines). Rotation at many different angular velocities of the molecules of both the excited and unexcited populations causes dephasing of the alignment or loss of the initial order. On a much longer timescale, this order may be recovered at the time of a rotational recurrence by rephasing of the alignment.

This is the intensity in the direction of an elastically scattered electron of wave vector \mathbf{k} , with momentum transfer \mathbf{s} , as defined above. The argument of the double summation represents interference between scattering from a pair of atoms at instantaneous internuclear separation \mathbf{r}_{ij} , and includes the atomic scattering amplitude $|f_i(s)|$ and atomic scattering phase $\eta_i(s)$ of each atom. The averaging indicated by the angle brackets must account for the fact that, in a real sample at any instant in time, the vector \mathbf{r}_{ij} will take on a range of values, characterized by vibrational and rotational distributions. Individual \mathbf{r}_{ij} 's will also evolve in time (see below). The dependence on t of temporally evolving quantities is indicated explicitly in Equation (1), as it is throughout the Article.

The distribution pertinent to the Equation (1) rotational, or orientational, average is the distribution in the *direction* of \mathbf{r}_{ij} . In the time-dependent problem, this distribution depends on the distribution of kinetically distinct rotational states (which we write $P_j(\mathbf{j})$, where \mathbf{j} is the rotational angular momentum vector in a molecule-fixed frame at $t=0$) as well as on the initial orientational distribution of molecules in the lab frame. It is the average over both of these distributions, represented by the term [Eq. (2)]:

$$F_{ij}(t; \mathbf{s}) = \langle e^{i\mathbf{s} \cdot \mathbf{r}_{ij}(t)} \rangle_{\text{Rot}}, \quad (2)$$

which is the focus of this paper. (We note that F is usually used for the structure factor in crystallography, which differs from the definition of F_{ij} given here; also l is used as an atomic index, instead of the usual j , in order to reserve the latter symbol for reference to rotational angular momentum.) The vibrational average will not be dealt with here, and all scattering calculations will be in the rigid-molecule limit, with fixed values of the lengths $r_{ij}=|\mathbf{r}_{ij}|$. For quantitative comparison with experiment, vibrational averaging of $F_{ij}(t; \mathbf{s})$ will be important to consider, but such averaging is not expected to alter the conclusions on the nature and scope of orientational effects reached from the model calculations carried out here. The normal effect of vibrational averaging is to broaden radial distributions, as discussed later.

Geometrical relationships used in carrying out the orientational average are defined in Figure 2, consistent with the notation of WZ.^[4] The electrons are incident along the laboratory z axis, and scattering from the sample volume, near the coordinate origin, is detected on a surface normal to this axis at a large positive z (see Figure 1). The direction of the absorption transition dipole moment, $\boldsymbol{\mu}_1$, for any selected molecule can be defined by spherical coordinates (Ω, Ψ) as shown. The direction of the wave vector \mathbf{k} of a scattered electron is specified in the same coordinate system by (θ, ϕ) , as shown in Figure 1. The angles Ω_{ij} and α define the direction relative to $\boldsymbol{\mu}_1$ of a particular internuclear separation, \mathbf{r}_{ij} , of the molecule. Rotational motion causes \mathbf{r}_{ij} , and thus also Ω_{ij} and α , to evolve in time.

The laser excitation, at time $t=0$, separates the sample at subsequent times into two subensembles—the excited and the unexcited—characterized by specific orientational distributions of their transition dipoles at $t=0$, $S_0^{\text{ex}}(\Omega, \Psi)$ and $S_0^{\text{un}}(\Omega, \Psi)$. Not only do these two molecular ensembles have

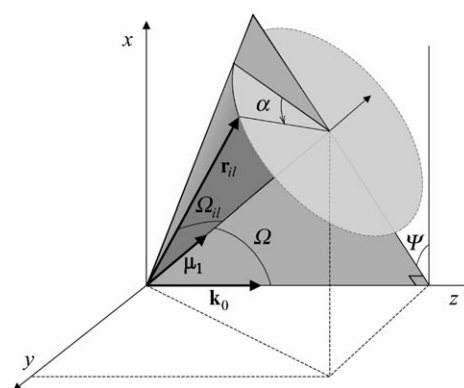


Figure 2. Geometry used in the calculation of anisotropic ultrafast electron diffraction of an internuclear separation \mathbf{r}_{ij} . The x,y,z axes represent a laboratory-fixed reference frame. The polar coordinates of the excitation transition dipole moment, $\boldsymbol{\mu}_1$, are Ω and Ψ and the wave vector of incident electrons, \mathbf{k}_0 , lies along the z axis. The angles Ω_{ij} and α specify the direction of \mathbf{r}_{ij} relative to $\boldsymbol{\mu}_1$. The plane defined by \mathbf{k}_0 and $\boldsymbol{\mu}_1$, represented by the large shaded right triangle, serves as a reference for measurement of the angle α in a plane normal to $\boldsymbol{\mu}_1$.

different initial spatial distributions, but their molecules have distinct structures and undergo different rotational dynamics, so they must be treated independently. The orientational distribution of transition dipoles at $t=0$, $\boldsymbol{\mu}_1(0)$, within each subensemble depends on the direction of the laser polarization vector $\boldsymbol{\varepsilon}$. In this paper we will assume that the laser is linearly polarization and that the excitation is weak enough to avoid saturation effects; therefore the distribution of the excited population will be proportional to $(\boldsymbol{\varepsilon} \cdot \boldsymbol{\mu}_1(0))^2$. With the total population normalized to unit amplitude over the sphere, that is, [Eq. (3)]:

$$\frac{1}{4\pi} \int_0^\pi \int_0^{2\pi} (S_0^{\text{ex}}(\Omega, \Psi) + S_0^{\text{un}}(\Omega, \Psi)) \sin \Omega \, d\Psi \, d\Omega = 1, \quad (3)$$

and a relative excitation yield of f^{ex} , the distribution of the excited population is given by Equation (4):

$$S_0^{\text{ex}}(\Omega, \Psi) = 3f^{\text{ex}} \cdot (\hat{\boldsymbol{\varepsilon}} \cdot \hat{\boldsymbol{\mu}}_1(0))^2, \quad (4)$$

where $\hat{\boldsymbol{\varepsilon}}$ and $\hat{\boldsymbol{\mu}}_1$ are unit vectors in the directions of $\boldsymbol{\varepsilon}$ and $\boldsymbol{\mu}_1$. The unexcited distribution is the complement to this [Eq. (5)]:

$$S_0^{\text{un}}(\Omega, \Psi) = 1 - 3f^{\text{ex}}(\hat{\boldsymbol{\varepsilon}} \cdot \hat{\boldsymbol{\mu}}_1(0))^2, \quad (5)$$

where it is understood that f^{ex} is always less than $1/3$.

The laser polarization vector can be restricted to lie in the xz plane without loss of generality. If the angle it forms in this plane with the z axis is δ , $(\hat{\boldsymbol{\varepsilon}} \cdot \hat{\boldsymbol{\mu}}_1(0))^2$ can be expressed as [Eq. (6)]:

$$(\hat{\boldsymbol{\varepsilon}} \cdot \hat{\boldsymbol{\mu}}_1(0))^2 = \cos^2 \delta \cos^2 \Omega + 2 \cos \delta \sin \delta \cos \Omega \sin \Omega \cos \Psi + \sin^2 \delta \sin^2 \Omega \cos^2 \Psi. \quad (6)$$

Because of the initial sample isotropy and the nature of the excitation process, within the ensemble of molecules having a given transition dipole direction (Ω, Ψ) , both the excited and unexcited subensembles must have cylindrical symmetry about $\mu_1(0)$ at all time. Thus, the distribution of \mathbf{r}_{ij} will always be uniform in α .

With this in mind, the average over initial molecular orientation, which is one part of the rotational average that appears in the scattering expression, Equation (1), can be written as Equation (7):^[4]

$$F_{ij}^{\delta, \text{ex/un}}(t; \mathbf{s}; \mathbf{j}) = 1/4\pi \int_0^\pi \int_0^{2\pi} S_0^{\text{ex/un}}(\Omega, \Psi) \left[\frac{1}{2\pi} \int_0^{2\pi} e^{i\mathbf{s} \cdot \mathbf{r}_{ij}(t)} d\alpha \right] \sin \Omega d\Psi d\Omega. \quad (7)$$

Here the variable \mathbf{j} indicates that this expression applies to a specific rotational state population since the functional form of $\mathbf{r}_{ij}(t)$ depends on the rotational state. With each rotational state making a contribution to electron scattering in proportion to its population, $P_j(\mathbf{j})$, the final step in the rotational average can be written as Equation (8):

$$F_{ij}(t; \mathbf{s}) = \left(\sum_{\mathbf{j}} P_j(\mathbf{j}) F_{ij}(t; \mathbf{s}; \mathbf{j}) \right) / \sum_{\mathbf{j}} P_j(\mathbf{j}) \equiv \langle F_{ij}(t; \mathbf{s}; \mathbf{j}) \rangle_{\mathbf{j}}. \quad (8)$$

The sum over \mathbf{j} in Equation (8), if viewed classically, becomes an integration over a continuous, Boltzmann distribution of angular momenta, or if viewed quantum-mechanically, is a sum over quantum states. The quantum-classical distinction is discussed further in the next section.

Based on Figure 2, the following expression can be derived for the laboratory frame Cartesian coordinates of the vector $\mathbf{r}_{ij}(t)$ [Eq. (9)]:^[4]

$$\mathbf{r}_{ij}(t) = r_{ij} \begin{bmatrix} (\sin \Omega_{ij}(t) \cos \alpha(t) \cos \Omega + \cos \Omega_{ij}(t) \sin \Omega) \cos \Psi - \sin \Omega_{ij}(t) \sin \alpha(t) \sin \Psi \\ (\sin \Omega_{ij}(t) \cos \alpha(t) \cos \Omega + \cos \Omega_{ij}(t) \sin \Omega) \sin \Psi + \sin \Omega_{ij}(t) \sin \alpha(t) \cos \Psi \\ \cos \Omega_{ij}(t) \cos \Omega - \sin \Omega_{ij}(t) \cos \alpha(t) \sin \Omega \end{bmatrix} \quad (9)$$

where typographical errors in Eq. (29) of ref. [4] have been corrected. The \mathbf{s} vector in the same coordinate frame is [Eq. (10)]:

$$\mathbf{s} = s (-\cos \phi \cos(\theta/2), -\sin \phi \cos(\theta/2), \sin(\theta/2)). \quad (10)$$

Upon substituting for $S_0^{\text{ex/un}}(\Omega, \Psi)$, \mathbf{s} , and \mathbf{r}_{ij} in Equation (7) by the above expressions, using Equation (6) for $(\hat{\epsilon} \cdot \hat{\mu}_1(0))^2$ in $S_0^{\text{ex/un}}(\Omega, \Psi)$, and carrying out the triple integration, we have obtained a solution in terms of infinite series summations, which can be evaluated numerically, and expressions in terms of standard functions have been found for the important cases of excitation polarization either parallel or perpendicular to \mathbf{k}_0 , as detailed below.

In the case referred to as *perpendicular excited*, that is, with the laser polarized perpendicular to the electron beam ($\delta = \pi/2$) and $S_0^{\text{ex}}(\Omega, \Psi) = 3f^{\text{ex}} \sin^2 \Omega \cos^2 \Psi$, the series solution is

found to be identical to the expression given by WZ (under their assumption of $f^{\text{ex}} = \frac{1}{3}$) [Eq. (11)]:

$$F_{ij}^{\perp, \text{ex}}(t; \mathbf{s}; \mathbf{j}) = 3f^{\text{ex}} \left\{ \frac{j_1(sr_{ij})}{sr_{ij}} - \left[\sin^2 \Omega_{ij}(t) + (2 - 3 \sin^2 \Omega_{ij}(t)) \cos^2 \frac{\theta}{2} \cos^2 \phi \right] \frac{j_2(sr_{ij})}{2} \right\} \quad (11)$$

where j_1 and j_2 are spherical Bessel functions,^[10] and $\cos^2(\theta/2)$ can also be written as $1 - s^2/(4k_0^2)$. All time dependence in this expression is contained in the angle Ω_{ij} , representing motion of \mathbf{r}_{ij} relative to the transition dipole $\mu_1(0)$. Similarly, a closed-form expression, found to be equal to the *parallel excited* case ($\delta = 0$, $S_0^{\text{ex}}(\Omega, \Psi) = 3f^{\text{ex}} \cos^2 \Omega$) result, is [Eq. (12)]:

$$F_{ij}^{\parallel, \text{ex}}(t; \mathbf{s}; \mathbf{j}) = 3f^{\text{ex}} \left\{ \frac{j_1(sr_{ij})}{sr_{ij}} - \left[\sin^2 \Omega_{ij}(t) + (2 - 3 \sin^2 \Omega_{ij}(t)) \sin^2 \frac{\theta}{2} \right] \frac{j_2(sr_{ij})}{2} \right\}. \quad (12)$$

As expected, $F_{ij}^{\perp, \text{ex}}(t; \mathbf{s}; \mathbf{j})$, for which ϵ is parallel to the x axis, shows a dependence on the azimuthal scattering coordinate ϕ which is symmetric with respect to the xz plane, while $F_{ij}^{\parallel, \text{ex}}(t; \mathbf{s}; \mathbf{j})$ is independent of ϕ .

It is intuitively obvious that, if the transition dipole distribution of a molecular ensemble is isotropic, such as for the total sample at $t=0$, then the distribution of any \mathbf{r}_{ij} in that ensemble is also isotropic. The form of $F_{ij}(\mathbf{s})$ for such an isotropic sample is simply $j_0(sr_{ij}) = \sin(sr_{ij})/sr_{ij}$, when the population is taken as 1 ($S_0(\Omega, \Psi) = 1$). From this observation and the form of $S_0^{\text{ex}}(\Omega, \Psi)$ and $S_0^{\text{un}}(\Omega, \Psi)$ it is easily seen that [Eq. (13)]:

$$F_{ij}^{\delta, \text{un}}(t; \mathbf{s}; \mathbf{j}) = j_0(sr_{ij}) - F_{ij}^{\delta, \text{ex}}(t; \mathbf{s}; \mathbf{j}) \quad (13)$$

for any value of δ , where $-F_{ij}^{\delta, \text{ex}}(t; \mathbf{s}; \mathbf{j})$ represents missing diffraction from that segment of the population of the ground state that was excited by the laser pulse. Its time dependence is therefore determined in this case by the rotational motion of the ground state, despite the ex label.

As a check on Equations (11) and (12), one may note that an isotropic distribution of transition dipoles of total population 1 results by adding the distributions created by three hypothetical excitations with ϵ along the three Cartesian axes, each with $f^{\text{ex}} = 1/3$. It must therefore be true that [Eq. (14)]:

$$F_{ij}^{\parallel, \text{ex}}(t; \mathbf{s}; \mathbf{j}) + F_{ij}^{\perp, \text{ex}}(t; \mathbf{s}; \mathbf{j}) + F_{ij}^{\perp, \text{ex}}(t; \mathbf{s}; \mathbf{j}) = j_0(sr_{ij}). \quad (14)$$

This result is easily confirmed from Equations (11) and (12) using the properties of the spherical Bessel functions, when it is recognized, from symmetry, that rotation of ϵ from the x to the y axis will simply change the $\cos^2 \phi$ factor in $F_{ij}^{\perp, \text{ex}}(t; \mathbf{s}; \mathbf{j})$ to $\sin^2 \phi$ in $F_{ij}^{\perp, \text{ex}}(t; \mathbf{s}; \mathbf{j})$.

Equations (11), (12), and (13) allow one to calculate the electron diffraction pattern from excited and unexcited subensem-

bles of a sample irradiated by a femtosecond pulse, accounting for the orientational anisotropy imposed on the distribution of $\mu_1(0)$ by the light field, for a given rotational state population, since $\sin^2 \Omega_{ij}(t)$ is determined by the rotational motion of the molecules in question. For a real sample with a distribution of rotational states, the j average of Equation (8) must be carried out on the expressions in Equations (11) or (12) to obtain $F_{ij}(t; \mathbf{s})$. When this is done, the only quantity that depends on j , $\sin^2 \Omega_{ij}(t)$, is simply replaced by $\langle \sin^2 \Omega_{ij}(t) \rangle_j$, for example, [Eq. (15)]:

$$F_{ij}^{\parallel, \text{ex}}(t; \mathbf{s}) = 3f^{\text{ex}} \left\{ \frac{j_1(sr_{ij})}{sr_{ij}} - \left[\langle \sin^2 \Omega_{ij}(t) \rangle_j + (2 - 3 \langle \sin^2 \Omega_{ij}(t) \rangle_j) \sin^2 \frac{\theta}{2} \right] \frac{j_2(sr_{ij})}{2} \right\} \quad (15)$$

For $\langle \sin^2 \Omega_{ij}(t) \rangle_j$ one may write:

$$\langle \sin^2 \Omega_{ij}(t) \rangle_j = 1 - \langle \cos^2 \Omega_{ij}(t) \rangle_j = 1 - \langle [\hat{\mu}_1(0) \cdot \hat{r}_{ij}(t)]^2 \rangle_j, \quad (16)$$

where $\hat{r}_{ij}(t) = \mathbf{r}_{ij}(t)/r_{ij}$, that is, it can be expressed in terms of the average value of the square of the time correlation function of two unit vectors fixed to the molecular frame. The same is true for the polarization anisotropy [Eq. (17)]:

$$r(t) = 0.4 \langle P_2[\hat{\mu}_1(0) \cdot \hat{\mu}_2(t)] \rangle_j = 0.6 \langle [\hat{\mu}_1(0) \cdot \hat{\mu}_2(t)]^2 \rangle_j - 0.2 \quad (17)$$

where $\hat{\mu}_2$ is a unit vector in the direction of a probe transition dipole and $P_2(x) = 0.5(3x^2 - 1)$ is the second-order Legendre polynomial. Thus, one may write [Eq. (18)]:

$$\langle \sin^2 \Omega_{ij}(t) \rangle_j = 1 - \frac{5}{3} \langle r(t) \rangle_{\hat{\mu}_2 = \hat{r}_{ij}} + 0.2 \quad (18)$$

from which it is clear that the complete calculation of a time-resolved diffraction signal requires the equivalent of calculating the time-resolved anisotropies for probe dipoles parallel to each atom pair in the molecule.

When Equation (18) is inserted in Equation (15) and its equivalent for $F_{ij}^{\perp, \text{ex}}(t; \mathbf{s})$, some rearrangement of terms leads to the following simple expressions [Eqs. (19) and (20)]:

$$F_{ij}^{\parallel, \text{ex}}(t; \mathbf{s}) = f^{\text{ex}} \left\{ j_0(sr_{ij}) + \frac{5}{2} \left(1 - 3 \sin^2 \frac{\theta}{2} \right) j_2(sr_{ij}) r(t) \right\}_{\hat{\mu}_2 = \hat{r}_{ij}} \quad (19)$$

$$F_{ij}^{\perp, \text{ex}}(t; \mathbf{s}) = f^{\text{ex}} \left\{ j_0(sr_{ij}) + \frac{5}{2} \left(1 - 3 \cos^2 \frac{\theta}{2} \cos^2 \phi \right) j_2(sr_{ij}) r(t) \right\}_{\hat{\mu}_2 = \hat{r}_{ij}} \quad (20)$$

These show that the electron scattering can be decomposed into an isotropic part, $j_0(sr_{ij})$, and a part proportional to the anisotropy of \mathbf{r}_{ij} , both of which are scaled by the population factor f^{ex} . It is now interesting to compare the above equations for anisotropic diffraction to that describing the physical population after photoexcitation. It can be shown for the case at hand (of molecular populations created by unsaturated excitation by linearly polarized light of an electric dipole transition)

that the excited-state distribution of any internuclear separation is given at all times t by Equation (21):

$$S^*(t; \Theta, \Phi) = f^{\text{ex}} [1 + 5 r(t) P_2(\cos \Theta)], \quad (21)$$

where Θ and Φ are polar coordinates about the excitation polarization, ϵ . Note that Θ and Φ are equal to Ω and Ψ only for ϵ along the z axis, and in that case $S^*(t; \Theta, \Phi)$, when applied to the transition dipole at $t=0$ ($r(t)=0.4$), reduces to parallel excited $S_0^{\text{ex}}(\Omega, \Psi)$ as defined earlier. Equation 21 is in the form of a multipole expansion^[9] of the orientational distribution. Comparison with Equations (19) and (20) shows that the isotropic and $r(t)$ dependent diffraction terms are each the scattering of a specific moment of the $\mathbf{r}_{ij}(t)$ distribution, as manifested for ϵ along z and x . In other words, the direct term-by-term correspondence between diffraction and spectroscopic anisotropies is expressed in Equations (19), (20), and (21).

According to Equation (21), the scalar quantity $r(t)$ uniquely determines the total orientational distribution of each $\mathbf{r}_{ij}(t)$; from this fact, it follows immediately that all orientational aspects of the calculation of electron diffraction patterns must be reducible to a calculation of anisotropies, as found above. Any established procedure for the calculation of time-resolved polarization anisotropies can be used, including fully quantum mechanical formulations for molecules of arbitrary shape.^[11,12] In the cases we will treat here, including dissociation reactions, the symmetric-top, semiclassical equations of refs. [7] and [8] will be used, and these are reviewed in the following section.

2.2. Rotational Coherence in Chemical Reactions

It was shown in the previous section that UED scattering patterns are dependent upon the time correlation of each internuclear separation vector in a molecule with the direction of its excitation transition dipole at $t=0$. This is an intrinsic property of the rotational motion of the molecule, depending only on its structure and the magnitude and initial direction of the rotational angular momentum vector in the molecular frame. From the standpoint of rotational dynamics, the structure is fully characterized by the three principal inertial axes and corresponding principal moments of inertia. Restricting our discussion here to rigid, symmetric-top molecules, two of the moments will be equal, and the inertial axis corresponding to the unique moment is referred to as the figure axis of the top. The rotational constants of the molecule about its figure axis and about any axis perpendicular to it, respectively, are designated B_{\parallel} and B_{\perp} , where $B_i = \hbar^2 / (4\pi I_i)$ for moment of inertia I_i .

The nature of the inertial, or unforced, rotational motion executed by a classical symmetric top is illustrated in Figure 3. The total angular momentum vector is \mathbf{j} , and its projection on the figure axis is \mathbf{k}_j . During the course of the motion, the angle of inclination, θ_j , of the figure axis to \mathbf{j} remains constant, which results in a constant magnitude for \mathbf{k}_j of $|\mathbf{j}| \cos \theta_j$. The body rotates about its figure axis at a fixed angular frequency^[13] [Eq. (22)]:

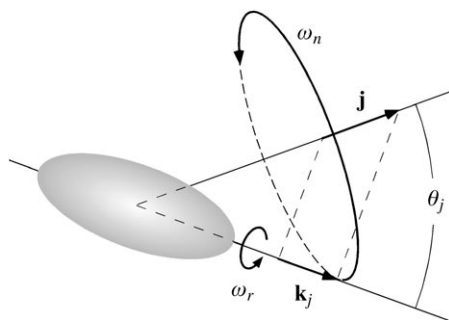


Figure 3. Rotational motion of a symmetric top. The vector \mathbf{j} is the total rotational angular momentum and \mathbf{k}_j is its projected component along the figure axis, which is inclined by a fixed angle, θ_j , from \mathbf{j} . ω_n and ω_r are the constant angular frequencies of nutation of the figure axis about \mathbf{j} and rotation of the molecule about the figure axis.

$$\omega_r = (1/I_{\parallel} + 1/I_{\perp}) |\mathbf{k}_j| = 4\pi(B_{\parallel} - B_{\perp}) |\mathbf{k}_j| / \hbar \quad (22)$$

and the figure axis nutates, or sweeps out a cone, at angular frequency [Eq. (23)]:

$$\omega_n = |\mathbf{j}|/I_{\perp} = 4\pi B_{\perp} |\mathbf{j}| / \hbar. \quad (23)$$

The quantum origin of time-dependent molecular orientation in photoexcited samples is the creation of excited states which are coherent superpositions of individual rotational quantum states—hence the designation of such a time-dependent behavior as rotational coherence. For symmetric-top molecules, the quantum states are labeled by the quantum numbers (j, k_j, m) , and the specific coherent rotational wave packet evolution is determined by the initial values of j and k_j only,^[14] assuming that all m levels are initially equally populated (\equiv isotropic sample). In all cases in which comparisons have been made, it has been found that the quantum behavior for a given (j, k_j) converges quantitatively to that given by the classical theory of symmetric-top rotation for $j = |\mathbf{j}|/\hbar$ and $k_j = |\mathbf{k}_j|/\hbar$, even at relatively low j values, and, with application of certain quantum corrections to the terms representing temporal modulations, at all times.^[8] Thus, all features of the state-resolved evolution may be understood by appealing to the classical picture. The transition from dealing with single states to the calculation of macroscopic, or ensemble-averaged, properties, as indicated in Equation (8), requires that the detailed properties of the \mathbf{j} distribution be specified. Herein, for the purpose of accurate reproduction of quantum recurrence behavior at longer times, all calculations are carried out for integer values of j and k_j and with the above-mentioned quantum corrections, which are listed at the end of this section. One should note, however, that at the early times in which we are mostly interested, the same orientation properties would also be found using a continuous, classical distribution, unless the sample were rotationally very cold.

The form of rotation of a molecule with particular values of j and k_j , as shown in Figure 3, can be translated into an explicit expression for the anisotropy $r(t)$ [Eq. (17)] when the directions in the molecular frame of the two unit vectors involved in the correlation are specified. This was done in the appendix of

ref. [8] for assumptions which will be adequate for the cases to be covered herein. Specifically, the two vectors, which, for the present purposes, will be referred to as $\hat{\mu}_1(0)$ and $\hat{r}_{ij}(t)$, are restricted to lie in a single plane containing the figure axis of the molecule. This condition is always satisfied if the transition dipole of the excitation is parallel to the figure axis, that is, for a parallel excitation transition. Also, \mathbf{j} is assumed to be uniformly distributed in the azimuthal coordinate of the molecular frame, as is always the case in a thermal ensemble of symmetric tops, since the rotational energy does not depend on this coordinate.

With the definitions $\omega_{no} = 4\pi B_{\perp}$ and $\omega_{ro} = 4\pi(B_{\parallel} - B_{\perp})$, where ω_{no} and ω_{ro} are referred to as the fundamental angular frequencies of nutation and rotation, and with $(\hat{\mu}_{1,\parallel}, \hat{\mu}_{1,\perp})$ and $(\hat{r}_{i,\parallel}, \hat{r}_{i,\perp})$ the Cartesian components of $\hat{\mu}_1(0)$ and $\hat{r}_{ij}(t)$ parallel and perpendicular to the figure axis in the plane common to all three vectors, one obtains the following expression [Eq. (24)] for the classical rotational-energy-resolved anisotropy (i. e. after averaging over the above-mentioned uniform azimuthal distribution):

$$\begin{aligned} r_{\hat{\mu}_1, \hat{r}_{ij}}(j, \theta_j, t) = & 1/10 \left(1/2 \hat{\mu}_{1,\perp}^2 - \hat{\mu}_{1,\parallel}^2 \right) \left(1/2 \hat{r}_{i,\perp}^2 - \hat{r}_{i,\parallel}^2 \right) \cdot \{ (3 \cos^2 \theta_j - 1)^2 \\ & + 12 \sin^2 \theta_j \cos^2 \theta_j \cos(j\omega_{no}t) + 3 \sin^4 \theta_j \cos(2j\omega_{no}t) \} \\ & + \hat{\mu}_{1,\perp}^2 \cdot \hat{r}_{i,\perp}^2 \{ \cos(2k_j\omega_{ro}t) \cdot (3/80 \sin^4 \theta_j + 3/20(1 - \cos^4 \theta_j) \cos(j\omega_{no}t) \\ & + 3/80(1 + 6 \cos^2 \theta_j + \cos^4 \theta_j) \cos(2j\omega_{no}t)) - \sin(2k_j\omega_{ro}t) \\ & \cdot (3/10 \cos \theta_j \sin^2 \theta_j \sin(j\omega_{no}t) + 3/20(\cos \theta_j + \cos^3 \theta_j) \sin(2j\omega_{no}t)) \} \\ & + 3/5 \hat{\mu}_{1,\perp} \cdot \hat{\mu}_{1,\parallel} \cdot \hat{r}_{i,\perp} \cdot \hat{r}_{i,\parallel} \{ \cos(k_j\omega_{ro}t) \cdot (3 \sin^2 \theta_j \cos^2 \theta_j \\ & + (2 - \sin^2 \theta_j - 4 \sin^2 \theta_j \cos^2 \theta_j) \cos(j\omega_{no}t) \\ & + (2 \sin^2 \theta_j - \sin^4 \theta_j) \cos(2j\omega_{no}t)) + \sin(k_j\omega_{ro}t) \\ & \cdot (2 \cos \theta_j (1 - 2 \cos^2 \theta_j) \sin(j\omega_{no}t) - 2 \cos \theta_j \sin^2 \theta_j \sin(2j\omega_{no}t)) \} \end{aligned} \quad (24)$$

where $\cos \theta_j = k_j/j$. This is Equation (4A) of ref. [8], but with correction of the typographical errors of one missing parenthesis and a missing 2 in the first $\sin(2j\omega_{no}t)$. To obtain $r(t)$, the rotational ensemble average must be completed, accounting for the distribution of population among rotational-energy levels [Eq. (25)]:

$$r(t) = \left(\sum_j P_j(j, \theta_j) r_{\hat{\mu}_1, \hat{r}_{ij}}(j, \theta_j, t) \right) / \sum_j P_j(j, \theta_j) \quad (25)$$

In the case of electron diffraction, the anisotropy of Equation (25) will be used in Equations (19) or (20) for every atom pair of the reactant and of the product, as indicated by the summations in Equation (1). For calculations for different atom pairs of a given molecule, only the values of $(\hat{r}_{i,\parallel}, \hat{r}_{i,\perp})$ change in Equations (24) and (25), and, thus, $r(t)$ for every such atom pair can be written as a sum of the form [Eq. (26)]:

$$r(t) = \left(1/2 \hat{r}_{i,\perp}^2 - \hat{r}_{i,\parallel}^2 \right) \cdot r_1(t) + \hat{r}_{i,\perp}^2 \cdot r_2(t) + \hat{r}_{i,\perp} \cdot \hat{r}_{i,\parallel} \cdot r_3(t) \quad (26)$$

for the same three functions $r_1(t)$, $r_2(t)$, and $r_3(t)$, found by

applying Equation (25) to those three terms of Equation (24) that are cofactors of the \hat{r}_{ij} -dependent coefficients of Equation (26). Using this relation, the total scattering of a molecule of any size can be calculated by carrying out the computationally demanding rotational averaging only once to determine $r_1(t)$, $r_2(t)$, and $r_3(t)$.

To complete the description of our calculations, there remains the determination of the rotational-energy-level distribution $P_j(j, \theta_j)$. In this Article, we must deal not only with intact molecules, but with dissociation products. For the first group, we assume all samples are characterized by a Boltzmann distribution. When carrying out the average represented by Equation (25), the summation over \mathbf{j} can be replaced by a double summation over integral j and k_j , in which case the proper energy-level population factor is [Eq. (27)]:

$$P_j(j, \theta_j) = (2j + 1) \cdot e^{-E_{rot}/k_b T}, \quad (27)$$

with $E_{rot} = B_{\perp} \cdot j(j + 1) + (B_{\parallel} - B_{\perp})k_j^2$. The normalization term $\sum P_j(j, \theta_j)$ then converges to the value of the rotational partition function [Eq. (28)]:

$$Q = [(\pi k_b^3 T^3) (h^3 B_{\parallel} B_{\perp}^2)^{-1}]^{1/2}. \quad (28)$$

For the products of dissociation, the calculation of $P_j(j, \theta_j)$ will be simplified by restricting consideration to dissociation of thermal samples of reactant molecules by prompt and impulsive loss of one atom upon excitation. These conditions require that the separation time be much shorter than the rotation period (prompt dissociation) and that fragment interactions in the exit channel be negligible. This case was treated in detail in ref. [7], and the angular momentum of the molecular product was shown to be composed of two independent contributions from (1) an impulsive torque and (2) the initial rotation of the reactant. The torque-induced angular momentum is zero if the separation impulse is directed toward the product molecule center of mass, or if no energy is released in the dissociation. In the examples that will be considered below, an impulse along the breaking bond satisfies the former condition and zero torque is taken as a reasonable assumption.

The second contribution to product rotation is the rotational angular momentum retained from the reactant. The general expression for retained angular momentum is [Eq. (29)]:^[7]

$$\mathbf{j}_r = \mathbf{I}^p (\mathbf{I}^R)^{-1} \mathbf{J} \quad (29)$$

where \mathbf{I}^p and \mathbf{I}^R are inertia tensors of the product and reactant molecules, and \mathbf{J} is the reactant angular momentum. For the present purposes, we will consider only the case of a reactant composed of a symmetric top product molecule plus one additional atom on its figure axis (which is taken as the z axis of a molecule-fixed frame), at distance z_A from its center of mass. The reactant is then also a symmetric top, and the figure axes of reactant and molecular product are parallel. In this case, Equation (29), in the molecule-fixed frame, reduces to Equation (30):

$$\mathbf{j}_r = \begin{pmatrix} \frac{I_{\perp}^p}{I_{\perp}^p + \mu z_A^2} & 0 & 0 \\ 0 & \frac{I_{\perp}^p}{I_{\perp}^p + \mu z_A^2} & 0 \\ 0 & 0 & 1 \end{pmatrix} \mathbf{J} \quad (30)$$

where μ is the reduced mass of the two product fragments (molecule and atom) and I_{\perp}^p is the product molecule moment of inertia about any axis perpendicular to its figure axis.

Under the conditions outlined above, the total angular momentum of the molecular product will be \mathbf{j}_r . Since \mathbf{J} is thermal and therefore uniformly distributed in the azimuthal coordinate about the figure axis, \mathbf{j} will be as well, which ensures that the use of Equation (24) is appropriate for the product anisotropies. (In cases where the torque is nonzero, or the reactant not a symmetric top, the assumption of Equation (24) of a uniform azimuthal distribution of \mathbf{j} may not be valid. In such cases, the product anisotropy must be calculated by the more general prescription given in ref. [7].) The energy-level populations, $P_j(j, \theta_j)$, required for Equation (25) are determined by attributing the Boltzmann populations for each \mathbf{J} of the reactant to the product of angular momentum \mathbf{j} as defined by Equation (30).

It was noted above that some adjustments need to be made for a classically derived expression such as Equation (24) to give quantitative agreement with the full quantum treatment at long times. These consist of replacing terms which oscillate at the classical frequencies with comparable terms oscillating at the correct quantum beat frequencies corresponding to the actual rotational-state level splittings. The following substitutions are made, with $f(x)$ representing either $\cos(x)$ or $\sin(x)$ [Eqs. (31a)–(31c)]:

$$f(j\omega_{n0}t) \rightarrow \frac{1}{2}[f(j\omega_{n0}t) + f((j+1)\omega_{n0}t)]; \quad (31a)$$

$$f(2j\omega_{n0}t) \rightarrow f((2j+1)\omega_{n0}t); \quad (31b)$$

and

$$f(k_j\omega_{r0}t) \rightarrow \frac{1}{2}[f((k_j + 1/2)\omega_{r0}t) + f((k_j - 1/2)\omega_{r0}t)]. \quad (31c)$$

3. Applications

In this section, some examples are provided to illustrate time dependence in UED due solely to orientational evolution. In all cases, we assume that laser and electron pulses are infinitely short and that the sample volume is infinitely small, so that the effective temporal response is a delta function, and that structural changes occur instantly at $t=0$. Thus, all changes in the diffraction pattern after $t=0$ are due to rotation. The initial sample is thermal, and 10% of reactant molecules absorb a photon from the laser pulse ($f^{\text{ex}}=0.1$). After $t=0$, the sample consists of 90% of the population as an unexcited oriented reactant ensemble and 10% as an excited oriented ensemble of

product molecules with appropriate nonthermal \mathbf{j} distribution. Dissociated atoms are assumed to contribute nothing to the molecular scattering.

An electron wavelength of 0.07 Å is used (≈ 30 keV). Calculations are done for an s range of 0 to 25 Å⁻¹, and resolution of 0.05 Å⁻¹. The appropriate expression for $F_{ij}(t; \mathbf{s})$ for each atom pair of both reactant and product is substituted in Equation (1), with the constant C set to a value of one, to obtain the molecular scattering intensity $I_M(t; \mathbf{s})$. Modified molecular scattering $sM(t; \mathbf{s})$ is calculated as [Eq. (32)]:

$$sM(t; \mathbf{s}) = \frac{sI_M(t; \mathbf{s})}{|f_a(\mathbf{s})||f_b(\mathbf{s})|}, \quad (32)$$

with normalization by the scattering factors of some arbitrary atom pair ab of the molecule. Difference patterns are referenced to the steady state scattering from the isotropic reactant population present before the arrival of the laser pulse: $\Delta sM(t; \mathbf{s}) = sM(t; \mathbf{s}) - sM(t < 0; \mathbf{s})$.

Radial distribution functions are calculated by Equation (33):

$$f(t; r) = \int_0^{s_{\max}} sM(t; \mathbf{s}) \exp(-k_d s^2) \sin(sr) ds \quad (33)$$

where an exponential damping term, with damping constant k_d , is used to suppress spurious oscillations. Integration extends to $s_{\max} = 25$ Å⁻¹. For an isotropic sample, every atom pair in a molecule gives rise to a peak in the radial distribution at a radial position approximately equal to the internuclear separation, with amplitude determined by the atomic scattering factors and the separation. The widths of different peaks would in a real sample be dependent on the mean amplitude of vibration associated with the particular atom pair, and also on the value chosen for the damping constant k_d in Equation (33). Here, where we have assumed rigid structures, we use $k_d = 0.012$ Å² and the resulting plots are similar to what one would expect for a slightly smaller k_d and a nonrigid molecule having a common vibrational amplitude for all its internuclear separations.

A simple case to consider, but one that also shows many of the important properties of anisotropic UED, is that of iodine absorption to a dissociative state via a parallel transition dipole. Electron diffraction from static ensembles of iodine molecules aligned by laser absorption has already been treated by WZ for a variety of assumptions, including excitation polarization both parallel and perpendicular to the electron beam. In the latter case, the scattering intensity varies with the azimuthal angle ϕ , as seen in Equation (20). For simplicity, we will restrict our consideration here to the parallel case, Equation (19), in which the cylindrical symmetry of the scattering pattern is preserved, and focus instead on the new element of time dependence.

The diffraction pattern of interest after $t=0$ is that of the parallel, unexcited iodine ground state, with $r_{I-I} = 2.666$ Å, since dissociation of excited molecules is considered instantaneous. To calculate this pattern, we use Equations (1), (8), (13),

and (19). As mentioned in connection with Equation (13), the anisotropy needed for Equation (19) is one involving the lost internuclear separation vectors, \mathbf{r}_{I-I} , of molecules of the ground-state iodine population that dissociate upon excitation by the laser, leaving a hole in the diffraction pattern [as indicated by the negative sign of Eq. (13)]. This $r(t)$ is shown in Figure 4. Because the transition dipole is parallel to the I-I

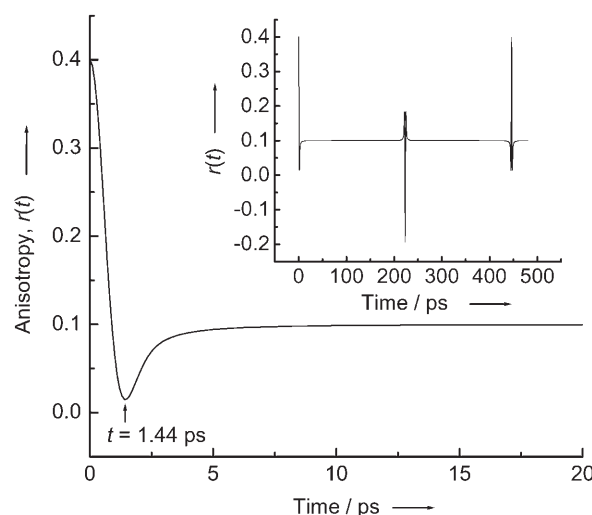


Figure 4. Time-resolved anisotropy of a virtual ground-state iodine population, at a single fixed structure ($B_{\perp} = 1.1206$ GHz), for femtosecond laser excitation via a transition dipole moment parallel to the I-I bond. The sample rotational temperature is 295° K. The inset shows the behavior on a longer timescale, revealing the first out-of-phase and in-phase rotational recurrences at 223.1 and 446.2 ps.

bond, the form of $r(t)$ is that typical of linear molecule rotational coherence for the ($||, ||$) dipole case. At $t=0$, the \mathbf{r}_{I-I} internuclear separation vectors of the excited population are in a cosine-squared distribution aligned along the laser polarization direction (laboratory z axis), and this distribution corresponds to the $r(0)$ value of 0.4. Thereafter, the orientation of the (now virtual) population dephases, as its individual molecules rotate with thermally ($T=295^{\circ}$ K) distributed angular momenta. The initial distribution of \mathbf{r}_{I-I} , however, imposes a permanent sine-squared distribution on the orientation of the angular momenta of the population because \mathbf{j} is perpendicular to the molecular axis ($\theta_j = 90^{\circ}$) for a linear molecule; thus even when fully dephased, the lost \mathbf{r}_{I-I} are not randomly oriented, in which case the value of $r(t)$ would be zero, but attain an asymptotic distribution with $r(t) = 0.1$.

A general characteristic of thermal rotational coherence that is evident in Figure 4 is the fact that $r(t)$ falls to a minimum (here at 1.44 ps) before reaching its asymptote. This feature is a remnant of the oscillations of the single energy level anisotropies that persists because dephasing takes longer, due to the limited width of the thermal angular momentum distribution, than required for molecules near the peak of the distribution to rotate through an angle approaching 90° . At longer

times, and periodically for as long as the sample remains collision-free, the distribution refocuses to give out-of-phase (sine-squared r_{\perp} distribution) and in-phase (cosine-squared r_{\perp} distribution) anisotropy recurrences, as determined by the quantum nature of the angular momentum and the specific circumstances which apply in this case.^[14] The first of each of these recurrences is shown in the inset of Figure 4. It should be noted that the case illustrated is that of a single rigid structure, while for a real room-temperature iodine sample, all molecules are not in the ground vibrational state and centrifugal distortion changes the bond length as a function of j . The resulting variation in moment of inertia in the sample causes recurrences to consist of multiple, broadened peaks,^[15] in contrast to the single sharp peaks shown in the Figure.

According to Equation (19), the anisotropy of Figure 4 is imprinted directly onto the electron diffraction patterns of the irradiated sample, as shown in Figure 5. We assume a 10% total

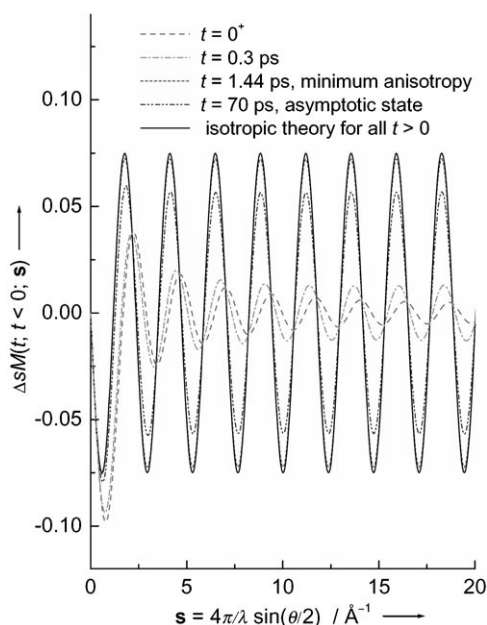


Figure 5. Modified molecular scattering difference plots at four selected times in the evolution of a room temperature ($T=295^\circ\text{K}$) iodine sample following 10% dissociation by a femtosecond laser pulse. The transition dipole moment is parallel to the I–I bond and the laser is polarized along the laboratory z axis (parallel to the electron beam). Also shown for comparison (and almost coincident with the 1.44 ps data) is the predicted $\Delta sM(t; t < 0; s)$ for all positive times assuming an isotropic and instantaneous depletion of 10% of the sample (solid line).

excitation yield, and calculate $\Delta sM(t; t < 0; s)$ at the characteristic times $t=0^+$, 0.3 ps, 1.44 ps and 70 ps, and compare with $\Delta sM(t > 0; t < 0; s)$ for a hypothetical isotropic excitation of 10% of the sample. Difference curves are used to represent the scattering because $sM(t; s)$ for a small excitation yield is dominated by the background ground state. Two iodine scattering factor amplitudes have been used in Equation (32) for this single atom pair, resulting in a simple sinusoidal form for isotropic dissociation [Eq. (34)]:

$$\Delta sM_{ij}^{iso}(t; t < 0; s) = \frac{-2f^{\text{ex}} \sin(sr_{ij})}{r_{ij}} \quad (34)$$

Two difference curves of Figure 5, $t=0^+$ and isotropic theory, can be compared to the two calculations labeled, respectively, excited and isotropic in Figure 5 of WZ, with, however a reversal of sign because the respective populations have been lost in the present case. Also note that the scattering losses represent equal populations for each curve in Figure 5, while the excited population was assumed to be 1/3 of the isotropic one by WZ.

The following points are evident from Figure 5. When the anisotropy with respect to the z -axis is positive and large, that is, when the lost atomic pairs are in a distribution preferentially oriented parallel to the electron beam (at $t=0^+$ and 0.3 ps), the $sM(t; s)$ difference curve decays quickly with s and is very strongly reduced relative to the isotropic case, except at low s . This apparent weakness of molecular scattering intensity for such high anisotropy distributions derives from the relatively rapid change of interference fringe spatial frequency with angle for small angles of tilt of r_{ij} from the z axis, leading to a dephasing with s of the constructive addition of oscillations contributed by different segments of the distribution. Thus, in an isotropic sample, most of the net molecular intensity for $s > 2 \text{ \AA}^{-1}$ derives from internuclear distances that are more nearly perpendicular than parallel to the electron beam. This basic orientation-dependent difference in scattering pattern is the source of all of the effects that will be seen for the parallel polarization cases discussed in this paper. When the anisotropy drops to its minimum value, $r(1.44 \text{ ps})=0.0146$, the difference signal closely approaches that of the isotropic excitation, for which $r(t) \equiv 0$. At longer time, the orientation of r_{\perp} of the completely rotationally-dephased virtual population of excited molecules again favors the z axis and hence shows a reduced scatter (smaller loss), with some distortion at low s .

It is also notable that the $\Delta sM(t; t < 0; s)$ curves at all times intersect at a series of common points. This phenomenon resembles that of spectroscopic isosbestic points and can be similarly explained. Each distribution given by Equation (21) can also be expressed as a conserved population f^{ex} divided in various ways between two fundamental distributions, $3 \cos^2 \Theta$ and $3/2 \sin^2 \Theta$. The value of $\Delta sM(t; t < 0; s)$ of the total distribution must then be constant at all points at which the $\Delta sM(t; t < 0; s)$ curves of these two fundamental distributions intersect, provided that f^{ex} is constant, as assumed here. Mathematically, these stationary points are easily recognized as the zeros of the coefficient of $r(t)$ in Eq. (19), which are simply the zeros of $j_2(sr_{ij})$.

Using Equation (33) and the $\Delta sM(t; t < 0; s)$ data of Figure 5, one may calculate the radial distribution difference curves, $\Delta f(t; t < 0; r)$, shown in Figure 6. These confirm the conclusions drawn above from the $\Delta sM(t; t < 0; s)$ plots, but also clearly display two additional characteristics. First, the apparent bond length distribution of the lost I_2 population, as indicated by the negative intensity in $\Delta f(t; t < 0; r)$, is extremely broad at very early time with maximum amplitude at an r value lower than the actual 2.666 Å bond length, and second, the asymp-

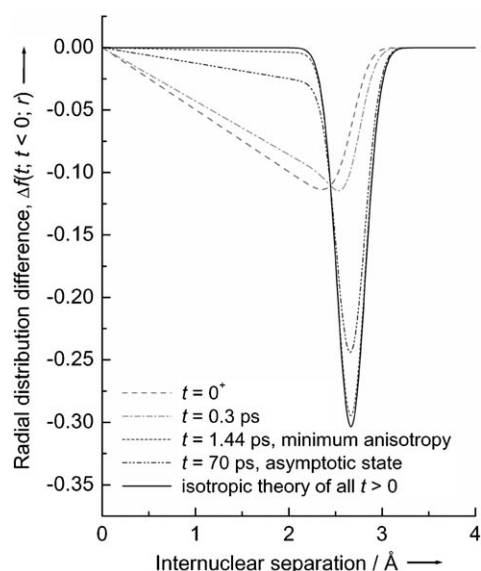


Figure 6. Radial-distribution-difference curves of parallel-excited iodine, derived from the scattering signals of Figure 5. A damping constant of $k_d = 0.012 \text{ \AA}^2$ was used.

otic $\Delta f(t; t < 0; r)$ peak is not only 20% smaller in peak amplitude than expected from the isotropic theory, but its line shape is also different, having a distinct tail extending to low r . Again, it is seen that the anisotropic UED signal very closely approximates the isotropic theory only near 1.44 ps, when the value of $r(t)$ reaches its minimum value. One stationary point appears in the $\Delta f(t; t < 0; r)$ plots, at $r = 2.4459 \text{ \AA}$ in this case (dependent on the value of k_d), which follows, as for $\Delta sM(t; t < 0; \mathbf{s})$, from a two-component description of the underlying distributions.

The detailed time evolution of the point of maximum absolute value on the $\Delta f(t; t < 0; r)$ curve is represented in Figure 7 by plots of both its position and its amplitude. Over the first 300 fs, the peak changes little in amplitude as it shifts to longer r . The amplitude then grows toward its maximum absolute value at 1.44 ps, at which time it also reaches a maximum in peak position, of 2.666 \AA , indicated by the dashed line. Both values then retreat from their maxima, with the peak position changing only very slightly, reaching an asymptotic value (at the resolution of the calculation) of 2.658 \AA by $\approx 5 \text{ ps}$. The relative reduction in the amplitude is much greater, and therefore it can be seen that a slight decay continues for tens of picoseconds (see Figure 7, inset), mirroring the evolution of the anisotropy of Figure 4.

Although the laser-induced change in I_2 population in the case under consideration is complete within the laser pulse at $t = 0$, the $\Delta sM(t; t < 0; \mathbf{s})$ and $\Delta f(t; t < 0; r)$ curves continue to change dramatically over a time range of several picoseconds due to evolving orientation, as shown in Figures 5, 6, and 7. One quantity that is found to accurately reflect only the population change is the integral of $r\Delta f(t; t < 0; r)$, which is also plotted in Figure 7. Combining the general expressions for $I_M(t; \mathbf{s})$ and $sM(t; \mathbf{s})$, with C in Equation (1) again set to one, the contribution of a single atom pair to $\Delta sM(t; t < 0; \mathbf{s})$ is [Eq. (35)]:

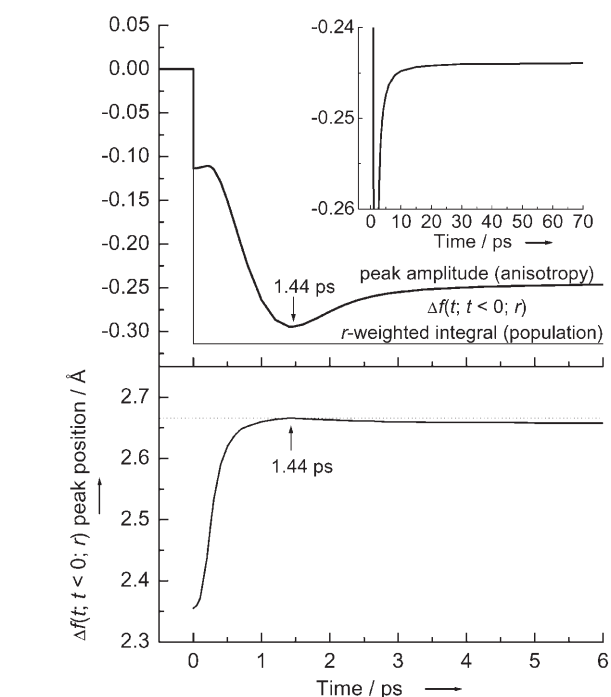


Figure 7. Time dependence of the position and amplitude of the radial-distribution-difference peak of parallel-excited iodine, for conditions described in the caption to Figure 5. While both quantities depend on the value of the constant k_d , their extremes always occur at 1.44 ps, the time of minimum anisotropy in Figure 4. Also shown is $\int_0^\infty r\Delta f(t; t < 0; r) dr$ as a function of time for the anisotropic dissociation. Convergence of the integrals was reached with an upper r limit of 4 \AA .

$$\begin{aligned} \Delta sM_{ij}(t; t < 0; \mathbf{s}) &= 2s \frac{|f_i(\mathbf{s})||f_j(\mathbf{s})|}{|f_a(\mathbf{s})||f_b(\mathbf{s})|} \\ &\cos(\eta_i(\mathbf{s}) - \eta_j(\mathbf{s})) (F_{ij}^{\delta, \text{ex}}(t; \mathbf{s}) + F_{ij}^{\delta, \text{un}}(t; \mathbf{s}) - j_0(sr_{ij})) \\ &= 2s \frac{|f_i(\mathbf{s})||f_j(\mathbf{s})|}{|f_a(\mathbf{s})||f_b(\mathbf{s})|} \cos(\eta_i(\mathbf{s}) - \eta_j(\mathbf{s})) (F_{ij}^{\delta, \text{ex}}(t; \mathbf{s})|_{\text{product}} - F_{ij}^{\delta, \text{ex}}(t; \mathbf{s})|_{\text{ground state}}) \end{aligned} \quad (35)$$

For the homonuclear diatomic, for which the influence of the scattering factors can be totally eliminated from the above equation, it can be shown under proper consideration of the damping and integration limits in Equation (33) that for either the parallel or perpendicular polarization case [Eq. (36)]:

$$\int_0^\infty r\Delta f(t; t < 0; r) dr = \pi (f_{\text{product}}^{\text{ex}} - f_{\text{ground state}}^{\text{ex}}), \quad (36)$$

where $f_{\text{product}}^{\text{ex}}$ and $f_{\text{ground state}}^{\text{ex}}$ are the yields of bound product atom pairs and loss of reactant atom pairs, respectively, that is, a contribution of πf^{ex} is associated with each term of $F_{ij}^{\parallel, \text{ex}}(t; \mathbf{s})$ or $F_{ij}^{\perp, \text{ex}}(t; \mathbf{s})$ in Equation (35), independent of r_{ij} , k_d , and the evolving orientational distribution of the relevant population.

For the example at hand, the value of the integral in Equation (36) jumps from 0 for $t < 0$ to -0.314159 for all $t > 0$ (Figure 7). This behavior reflects exactly an instantaneous dissociation of 10% of I_2 molecules, with $f_{\text{product}}^{\text{ex}} = 0$ since all excit-

ed molecules dissociate, and $f_{\text{ground state}}^{\text{ex}} = 0.1$. It should be noted that this equation remains valid under more general conditions than those assumed here, for example, for molecules in which the bond distance is not fixed and for reactions which are not instantaneous, in the latter case yielding a pure measure of the net percentage change in number of bound atom pairs in the sample, whether in the product or the reactant, at any point in time. For example, if an excitation changed the bond length but left the molecule intact, $f_{\text{product}}^{\text{ex}}$ would be equal to $f_{\text{ground state}}^{\text{ex}}$ and the integral would be zero. Of course, in the case of molecules on a slow dissociative trajectory, the point at which the separating atoms no longer constitute an effectively "intact" molecule, but instead contribute only to the incoherent atomic scattering background becomes a technical issue that must be addressed in the analysis, as is the limited range of s that is available from experiments.

As a final point, it should be noted that the consequences of rotational recurrences in the anisotropy (as seen in the inset of Figure 4) could, with sufficient time resolution, also be observed in UED. Since recurrence times are determined by molecular structure, their observation by UED could be used for structural measurements, as are recurrence observations by numerous other ultrafast spectroscopic techniques.^[11,12] To illustrate this possibility, $\Delta f(t; t < 0; r)$ has been calculated at the times of the out-of-phase and in-phase recurrences, and these are shown in Figure 8, with the steady state signal of Figure 6 replotted for comparison. (As noted in connection with the recurrences of Figure 4, two factors which must be considered in a real sample at finite temperature, the vibrational distribution and centrifugal distortion, have been ignored for these calculations.)

The scattering changes dramatically at each recurrence, almost doubling the $\Delta f(t; t < 0; r)$ peak at the out-of-phase re-

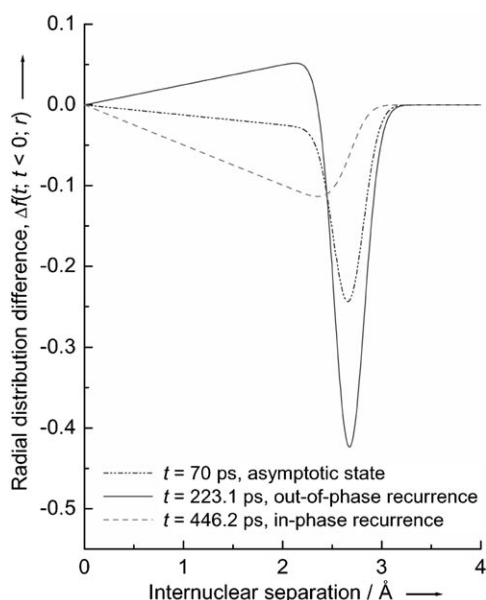


Figure 8. Radial distribution differences of parallel-excited iodine, at the times of an out-of-phase and an in-phase rotational coherence recurrence, compared with the steady-state signal from Figure 6. Other conditions are described in the caption to Figure 5.

currence, and returning to the $t=0^+$ appearance at the in-phase recurrence. However, the integral of Equation (36) remains equal to -0.314159 at these times as well, emphasizing that the change in scattering pattern reflects only reorientation of a fixed population. At the out-of-phase and in-phase recurrences, the dissociated molecules, if they had remained intact, would be in sine-squared and cosine-squared distributions, respectively, relative to the z axis, and thus largely perpendicular in the first case, and parallel in the second, to the electron beam, which results in the large discrepancy in the nature of the scattering.

Each of these recurrences, for which $r(t) = -0.2$ and 0.4 , respectively, corresponds to full occupation of one of the two fundamental distributions discussed above in connection with the existence of stationary points. This being the case, every characteristic property of the evolving distribution must always have a value intermediate to those associated with these two times. The anisotropy (Figure 4) represents one such property; likewise, all $\Delta f(t; t < 0; r)$ curves lie between limits set by $\Delta f(223.1 \text{ ps}; t < 0; r)$ and $\Delta f(446.2 \text{ ps}; t < 0; r)$ and can be expressed as appropriately weighted averages of the two, as follows from Equations (19), (32), and (33); for example, at the steady state ($r(t) = 0.1$), the weighting is equal and $\Delta f(70 \text{ ps}; t < 0; r)$ is the mean of $\Delta f(223.1 \text{ ps}; t < 0; r)$ and $\Delta f(446.2 \text{ ps}; t < 0; r)$, as is evident from Figure 8.

The positive amplitude at low r in $\Delta f(223.1 \text{ ps}; t < 0; r)$ is an interesting feature arising because the orientation of the *undissociated* molecules at that time is biased toward the z -axis. Their positive contribution to the radial distribution is therefore broadened, resulting in a larger hole at 2.666 \AA and positive difference at low r , just as the negative contribution of similarly oriented *missing* molecules is broadened at $t=0^+$.

In summary, the rotational coherence created by the femtosecond excitation is both responsible for the timescale of growth and evolution of the diffraction pattern and significantly affects the asymptotic, or steady state, scattering, while only population dynamics is reflected by the integral of $r\Delta f(t; t < 0; r)$. In this case, for example, the dramatic increase in amplitude of the negative peak in $\Delta f(t; t < 0; r)$ from $t=0$ to 1.44 ps reveals the average rate of rotation of the sample molecules rather than a change in the dissociated population. This temporal evolution could thus be used to determine the sample rotational temperature. Rotation and dephasing times of a thermal sample scale as $(T)^{-1/2}$, and rotational coherence behavior similar to that shown but on different timescales is to be expected at all temperatures for which the $j=0$ population is not a large fraction of the total.

From the preceding example, in which the orientation of a single bond and a single state is involved, we now turn to a more complex case, that of photodissociation of CF_3I . Here, we must account for multiple internuclear separations and two different molecules, CF_3I and CF_3 . We use the same ground state structure^[16] as used by WZ in their calculation for perpendicular laser polarization of diffraction by the unexcited population only. For a complete picture of anisotropic UED, we assume a 10% excitation yield via a parallel transition dipole (along the C–I bond) leading to instantaneous loss of the

iodine atom, and calculate the total scattering due to the unexcited thermal ground state CF_3I and the product CF_3 . The rotational distribution of CF_3 is that given by applying Equation (30) to the CF_3I thermal distribution, assuming that the product structure is the same when free as when bound within the reactant.

Figure 9 shows the radial distribution difference curves for the total diffraction signal at a series of different times, again compared to the isotropic theory calculation for 10% dissociation.

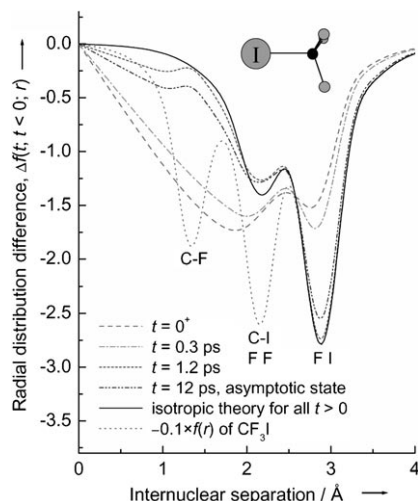


Figure 9. Radial-distribution-difference curves for anisotropic UED scattering of CF_3I dissociation to $\text{CF}_3 + \text{I}$ at four times. The laser polarization is parallel to \mathbf{k}_0 , $T = 295^\circ \text{K}$, and the transition dipole moment is parallel to the C–I bond. The structure of CF_3I is shown, and the structural parameters of Typke et al.^[16] for CF_3I were used in the calculations for both CF_3I and CF_3 . The solid curve is a calculation for the dissociation assuming isotropic distributions and the light dotted curve is a scaled radial distribution of the reactant only, labeled with the atom pair(s) responsible for each peak.

tion. Also plotted for reference is $-0.1 \times f(r)$ of an isotropic sample of CF_3I , indicating the relative amplitudes and positions associated with each of the four distinct internuclear separations, as labeled in the Figure, with the C–I bond and FF distance being almost equal ($r_{\text{CI}} = 2.141 \text{ \AA}$ and $r_{\text{FF}} = 2.154 \text{ \AA}$). The calculations account for the multiplicities for CF_3I of one C–I bond and three C–F, FI, and FF distances, and for CF_3 of three C–F and FF distances. In each case, two fluorine scattering-factor amplitudes were used in the calculation of $sM(t; s)$ [Eq. (32)]. Coincidence between the FI peak of the $\Delta f(t; t < 0; r)$ curve for isotropic dissociation theory for $t > 0$ and that of $-0.1 \times f(r)$ of CF_3I illustrates the 10% loss of FI atom pairs by dissociation, as expected. The isotropic dissociation curve shows a loss at the CI/FF peak of about half of the 10% reference, corresponding to loss of 10% C–I and no FF, while the fact that no peak appears at the C–F bond distance shows that isotropic dissociation causes no change in the total C–F distribution in the sample.

Considering now the four anisotropic $\Delta f(t; t < 0; r)$ curves in Figure 9, general features seen in the previous example for I_2 are again evident. The two internuclear separations that are lost, CI and FI, contribute negative peaks in $\Delta f(t; t < 0; r)$, but at $t = 0^+$, these have very different shapes in the anisotropic than

in the isotropic calculation, with the peak from the C–I bond being significantly shifted from the actual C–I bond distance of 2.14 \AA , as was true for the I–I bond of I_2 . Because both the C–I bond of CF_3I and the I–I bond of I_2 are coincident with their respective excitation dipole moments, the excited populations at $t = 0^+$ share identical cosine-squared distributions and comparable diffraction properties are expected. A smaller shift is seen in the FI peak of CF_3I because the FI nonbonded separations are inclined by 25.5° from the transition dipole and are therefore not as strongly aligned. Because both CI and FI peaks are severely broadened and overlapping, the apparent peak amplitudes at early time are not readily comparable to that of the I–I peak of I_2 . However, at steady-state conditions, represented here by the 12 ps data, the amplitudes of both of the $\Delta f(t; t < 0; r)$ peaks are again lower than expected from isotropic theory, as was the case for I_2 . Finally, there is again a point in the radial distribution difference curves, at $\approx 2.578 \text{ \AA}$, that is effectively stationary, though not exactly so as in the I_2 case. The involvement of many different distributions for different r_{ij} , and two different courses of time evolution in the ground and product state ensembles invalidates the simple form of the two component explanation advanced for iodine, but the close coincidence at a single point of all curves here is certainly suggestive of a general property. We will return to this point further below.

In addition to the presence of multiple bonds, another new element which plays a role here is the effect of the product orientation. The total population of CF and FF separations is not changed by dissociation, but the rotational motion executed by the segment of those populations belonging to CF_3 product molecules does change. At $t = 0^+$, the distributions of the total population of these separations remains isotropic, as evidenced by the fact that $\Delta f(0^+, t < 0; r)$ shows no distortion in the vicinity of the C–F bond distance of 1.33 \AA . By 1.2 ps and in the steady state behavior, however, a positive-going deviation from the smooth trend of $\Delta f(t; t < 0; r)$ has appeared. (The time of 1.2 ps was chosen for the calculations because the anisotropies of the figure axes of both CF_3I and CF_3 are near their minimum values at this point, which is thus comparable to 1.44 ps for I_2 . The general appearance of these anisotropies is similar to that of I_2 in Figure 4, though they have different asymptotic values because of differences in molecular shape and j distribution.)

This effect is understood by considering Equation (30). The component of angular momentum along the figure axis (molecule-fixed z axis) is conserved from CF_3I (J) to CF_3 (j), while the perpendicular components are greatly reduced (by about a factor of six). Fragmentation, therefore, increases the average value of k_j/j , which corresponds to a decrease in θ_j , and a tighter cone of nutation, as shown in Figure 3. A reduced nutation cone means that the internuclear separation vectors of product molecules have a range of motion reduced from that which would have applied had the molecule remained intact. Since the transition dipoles of excited molecules, and therefore, in this case, the CF_3 figure axes are strongly aligned at $t = 0^+$, they will tend to remain unusually close to the laser polarization, or laboratory z axis, at all time, corresponding to a high

anisotropy $r(t)=0.2$ at the asymptote with a minimum value of 0.14 at 1.2 ps). Since r_{CF} is almost perpendicular to the figure axis, the r_{CF} 's in CF_3 will be preferentially oriented perpendicular to the z axis and to k_0 , and thus will give enhanced molecular scattering, producing a positive difference peak.

The same reasoning applies to r_{FF} implying that a positive peak due to the FF atom pairs of the product population reduces the amplitude of the overlapping negative CI peak. Such a reduction might be revealed by a comparison of the anisotropic CI/FF and FI peak amplitudes relative to those of the isotropic theory. At the steady state (12 ps), ground-state anisotropy effects, such as the expected low r tail of the FI peak and the fact that the CI ground-state anisotropy is greater than that of FI, complicate the situation, but at 1.2 ps, $r(t)$ for the ground state approaches zero ($|r(t)| \leq 0.013$ for all ground-state atom pairs), so ground-state differences from isotropic theory should be very small (cf. $I_2 \Delta f(t; t < 0; r)$ at 1.44 ps in Figure 6). The large discrepancy at CI/FF from the isotropic theory (reduction of 9.8% vs. 1.6% at FI) at 1.2 ps can therefore only be a product effect, consistent with a positive FF contribution of amplitude comparable to that which is evident for CF at the same time.

To reveal more clearly the role of product orientation, the product- and ground-state contributions to the total $\Delta f(t; t < 0; r)$ have been plotted separately in Figure 10 for anisotropic dissociation at 1.2 ps and for the isotropic dissociation at $t > 0$. These contributions are displayed in the form of $f(t; r)$ for the product and $\Delta f(t; t < 0; r)$ for the ground state. As reasoned above, the anisotropic ground state distribution is very similar to the isotropic one, with minor discrepancies of opposite sign

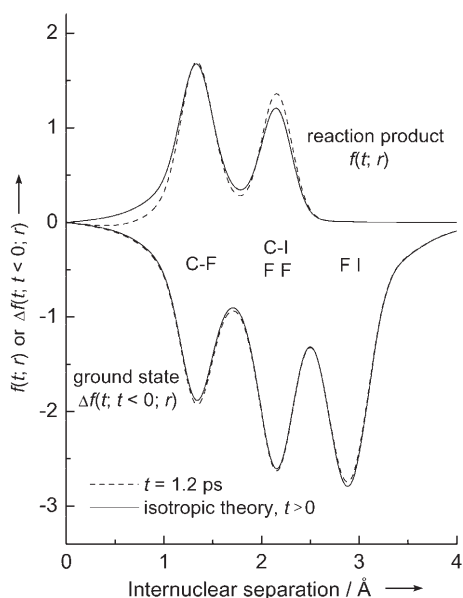


Figure 10. Separate reaction-product (CF_3) and ground-state contributions to two of the radial-distribution-difference curves of Figure 9. The reactant $f(r)$ was subtracted from the ground-state distributions, while $f(t; r)$ is plotted for the products without subtraction. The isotropic ground state $\Delta f(t > 0; t < 0; r)$ is equal to $-0.1 \times f(r)$ of the reactant, as plotted in Figure 9. The labels identify the atom pairs associated with each peak.

for internuclear separation vectors approximately parallel (FI and CI) and perpendicular (FF and CF) to the figure axis. Larger differences appear in the two peaks of the product radial distributions, with the amplitudes of both peaks of the anisotropic calculation being larger, relative to the adjacent baseline, than those of the isotropic case. Since the product CF and FF peaks exactly cancel the corresponding dips in the ground state $\Delta f(t; t < 0; r)$ for the isotropic case, it follows that the larger anisotropic product peaks leave a net positive contribution for those atom pairs in the total $\Delta f(t; t < 0; r)$ (Figure 9). The slightly negative baseline at low r in the anisotropic product $f(t; r)$ recalls the effect of opposite sign seen at the out-of-phase recurrence of I_2 (Figure 8) where the distribution of lost molecules was biased toward alignment with the xy plane as are the product CF and FF separations of the anisotropic calculation here. It is the negative low r tail of the product FF peak that causes the total anisotropic 1.2 ps $\Delta f(t; t < 0; r)$ of Figure 9 to lie below the isotropic curve at the C–F bond distance.

For I_2 , with a single atom pair, the integral in Equation (36) provided an orientation-independent measure of the change in bound population. For the CF_3I dissociation, ten atom pairs must be considered, and the atomic scattering factors are eliminated from Equation (35) only for the three FF atom pairs. Thus, it is remarkable that the r -weighted integral of the total $\Delta f(t; t < 0; r)$ is again independent of orientation, despite large differences among the anisotropic $\Delta f(t; t < 0; r)$ curves. Given that the Gaussian damping factor applied to $\Delta sM(t; t < 0; s)$ in Equation (33) does not effect the value of the integral in Equation (36), the influence of scattering factors can be understood under the condition that the s -dependence that they introduce into $\Delta sM_i(t; t < 0; s)$, can be decomposed into a weighted sum of Gaussians centered at $s=0$, that is, [Eq. 37]:

$$\frac{|f_i(s)||f_j(s)|}{|f_a(s)||f_b(s)|} \cos(\eta_i(s) - \eta_j(s)) = \sum_n \alpha_n e^{-k_n s^2}. \quad (37)$$

It then follows immediately that the contribution made to the integral of $r\Delta f(t; t < 0; r)$ by each atom pair that suffers a net loss of population from reactant to product is [Eq. (38)]:

$$-\sum_n \alpha_n \pi f^{\text{ex}} = -\frac{|f_i(0)||f_j(0)|}{|f_a(0)||f_b(0)|} \cos(\eta_i(0) - \eta_j(0)) \pi f^{\text{ex}}, \quad (38)$$

where f^{ex} is the fractional loss of population. In the dissociation of CF_3I , the sum of these quantities for the three FI and one CI atom pairs is -7.39755 , which is equal to the value obtained by numerical integration (from $r=0$ to 8 \AA) of each r -weighted $\Delta f(t; t < 0; r)$ curve of Figure 9, and also for radial distributions calculated with other values of k_0 . Thus the proportionality to f^{ex} is maintained, and the constant value indicates that, in this case, the population of bound atom pairs does not change after the initial loss occurs at $t=0$.

As a final example of anisotropic UED, we consider the case of CH_3I dissociation. The treatment of this problem is very similar in most respects to that of CF_3I , with the distinction that, unlike CF_3 , which was fixed at its reactant structure upon dissociation, the CH_3 structure will change from reactant to frag-

ment. CH_3I and CH_3 structural parameters are taken from Herzberg.^[17] A 10% excitation yield with transition dipole parallel to the C–I bond is again assumed, and $P_j(j, \theta_j)$ for product CH_3 is given by Equation (30) using a value of $P_{\perp}^p = 1.952 \text{ amu \AA}^2$ based on the structure of CH_3 within CH_3I . The small size of this moment of inertia relative to $\mu z_A^2 = 53.41 \text{ amu \AA}^2$ leads to a very high residual anisotropy of the product figure axis, of ≈ 0.36 . Given the low values of j_r , however, this is a case in which caution should be exercised in relying on the quantitative accuracy of the semiclassical treatment applied.

Time-resolved radial-distribution difference curves for anisotropic and isotropic dissociation theory, and the isotropic CH_3I ground state $f(r)$, were calculated using two hydrogen scattering factor amplitudes for the normalization in Equation (32). These are plotted in Figure 11. With the HH separation absent due to the weak electron scattering of hydrogen, the CI and HI internuclear separations lost to dissociation are both free of overlap with any observable product internuclear separation.

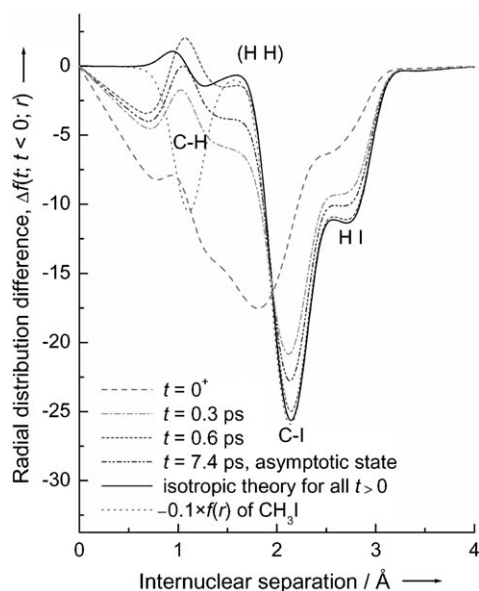


Figure 11. Radial-distribution-difference curves of anisotropic UED scattering of CH_3I dissociation to planar $\text{CH}_3 + \text{I}$ at four times. The laser polarization is parallel to \mathbf{k}_0 , $T = 295^\circ\text{K}$, and the transition dipole moment is parallel to the C–I bond. Structural parameters used for CH_3I and CH_3 are those given by Herzberg.^[17] The solid curve is a calculation for the dissociation assuming isotropic distributions and the light dotted curve is a scaled radial distribution of the reactant only, labeled with the atom pair responsible for each peak. (No peak is seen at the HH internuclear separation of 1.82 Å)

Thus, the CI and HI peaks of the isotropic theory $\Delta f(t > 0; t < 0; r)$ coincide fully with $-0.1 \times f(r)$ of CH_3I . A slight change in C–H bond length upon dissociation, from 1.106 Å to 1.079 Å, produces a derivative line shape in the isotropic theory $\Delta f(t > 0; t < 0; r)$ centered at 1.09 Å.

The general features of the time-dependent anisotropic data shown in Figure 11 are by now familiar: negative contributions to $\Delta f(t; t < 0; r)$ for the two lost separations, CI and HI, with severely broadened peaks at $t = 0^+$ that evolve over time to reach an asymptotic steady state with amplitudes smaller than

those of the isotropic theory; a pronounced shift of the CI peak at $t = 0^+$; and a positive peak at the C–H bond distance at long time due to high product anisotropy. Since there is no product interference in this case, the percentage reductions in the anisotropic relative to the isotropic calculation of the CI and HI negative peaks are very similar to each other, both at the time of minimum ground state anisotropy, $t = 0.6 \text{ ps}$, (reduction of $\approx 2\%$) and at the steady state (11%).

Among the differences between the CH_3I calculations and those of CF_3I is the shorter time required to reach either the minimum ground state anisotropy (0.6 ps vs. 1.2 ps) or the steady-state condition, represented here by the data at 7.4 ps, due to the smaller moments of inertia of CH_3I . There is also now structure due to the C–H bonds in $\Delta f(t; t < 0; r)$ at $t = 0^+$ and 0.3 ps while C–F of CF_3I made no contribution at such early times. At $t = 0^+$, this difference is totally due to the change in product structure which has been assumed here. Not only does the bond length change as noted above, but the orientation of each C–H bond shifts 17.7° from its position in the reactant ($\angle \text{ICH} = 107.7^\circ$) to the planar geometry of the product, leading to an initial sine-squared distribution relative to the z-axis. Such a distribution is optimum for enhancing the radial distribution amplitude at $r = r_{ij}$, as shown by the strong 2.666 Å peak in $\Delta f(t; t < 0; r)$ at the out-of-phase recurrence of I_2 (Figure 8), so the total CH signal exceeds that of the reference isotropic distribution, adding a positive contribution to the derivative shape arising from the change in bond length. Note that the bond angle change has no direct effect on the isotropic theory: the isotropic $\Delta f(t; t < 0; r)$ reflects the change in bond-length only.

At $t = 0.3 \text{ ps}$, the strong positive C–H peak that appears in CH_3I $\Delta f(t; t < 0; r)$ is in marked contrast to the absence of a C–F peak at the same time for CF_3I (Figure 9). Contributing to this difference is not only the change in structure, but also the influence of the high product anisotropy which is revealed earlier due to the faster rotation of the hole in the ground state CH_3I distribution. The fact that the CH_3 anisotropy is much higher than that of CF_3 (see above) is also a factor in producing relatively more prominent positive peaks at 0.3 ps and all later times.

The integral of $r\Delta f(t; t < 0; r)$ for each $\Delta f(t; t < 0; r)$ in Figure 9 is found equal to -43.477 , again reflecting the fact that no population change occurs after $t = 0$. The small hydrogen atomic scattering factor amplitudes used in Equation (32), compared to the carbon and iodine factors which appear in $I_m(t; s)$, are responsible for the large value of this integral compared to that for an equal dissociation yield of CF_3I . However, the numeric value in this case differs slightly from that (-44.053) found by assuming the validity of Equation (38). The condition underlying Equation (38), although sufficient, is thus not necessary to ensure orientation independence of the integral. While a fuller investigation is needed of the conditions for validity of this property, the high degree of consistency for the two polyatomic cases given here suggest a broad generality.

Similarly, the existence also for CH_3I of a near-stationary point in $\Delta f(t; t < 0; r)$ supports our earlier observation that such points apparently are an intrinsic feature of anisotropic UED, at

least under the specific set of conditions assumed for the examples in this work. As noted earlier for iodine, one requirement for the existence of the stationary points of $\Delta sM(t; t < 0; s)$ or $\Delta f(t; t < 0; r)$ for that simple system is a constant population; conversely, the value at such a point is a pure measure of population, independent of anisotropy, and could, at least in theory, fill the same role as the integral of $r\Delta f(t; t < 0; r)$. Exploring such possibilities by determining the origin and properties of these points, including any restrictions on the conditions under which they arise, is among the objectives of ongoing work in our laboratory.

4. Conclusions

Herein, we have treated the effect of the rotation of oriented molecular ensembles on the temporal evolution of diffraction on the actual ultrafast timescale of the rotational motion. In particular, we considered the most common case for inducing anisotropic molecular orientation, excitation by polarized pulsed laser beams, and incorporated the concepts of rotational coherence of molecules subject to free rotation under collisionless conditions. We invoked the classical dynamics of rotation to determine the time dependence of the orientational distributions of internuclear separation vectors, r_{ij} , for which molecular scattering intensities were calculated. As shown in our work on rotational coherence,^[8] such distributions very closely approximate the probability distributions of quantum wave packets created by coherent excitation. The role of product orientation following prompt laser-induced dissociation reactions was also examined.

We found that the diffraction pattern depends on the polarization anisotropy of the separation vector, $r(t)|_{\hat{\mu}_2=\hat{r}}$, and derived a simple expression showing term-by-term the scattering contributions of the multipole expansion of the evolving r_{ij} orientational distribution. The diffraction pattern differs dramatically from isotropic theory when the absolute value of that anisotropy is large, notably near $t=0$ and rotational recurrence times. However, deviations from isotropic theory were also apparent for steady-state orientational distributions, which, in the absence of collisions, may display substantial residual anisotropies. These anisotropies were shown in certain cases to be magnified by the kinematics of dissociation, resulting in the appearance of positive peaks in the radial distribution difference curves without any population change associated with the internuclear separation in question. In the cases presented, both the value of the radial distribution difference function at certain specific stationary ("isosbestic") points and the integral of that function weighted by the separation variable r were found to be independent of the orientational evolution of the laser-aligned populations, and thus provided a picture of the time-dependence of the total population of bound atom pairs.

For chemical reactions we considered the case of prompt dissociation, for which all evolution of the diffraction depends solely on the timescale of orientation effects. In future work, we will consider the role of anisotropy for non-prompt reactions. The role of non-rigidity of real samples, with implications for reaction dynamics as well as vibrational amplitudes, must

also be addressed. Incorporating finite experimental pulse widths and sample volumes is necessary for comparing transient features of the diffraction patterns in theory and experiment. In this regard, the existence demonstrated here of steady-state or asymptotic differences between anisotropic and isotropic theory is particularly significant, since these will be detectible without severe restrictions on experimental time-resolution. In essence, they reflect simply the fact that isolated molecules remain in distinct spatial modes of rotational motion in the lab frame due to conservation of angular momentum, and the molecules in each such mode have characteristic time-averaged probabilities for both polarized light absorption and electron scattering. Such findings are important to experiments designed for steady-state orientation, such as those involving orientation by multipole electric fields.

It is already clear from the results presented here that it is essential to understand the practical consequences of anisotropic and time-dependent orientations for their exploitation in structural determinations and for the accurate interpretation of UED data, including extraction of rates of population change and reaction yields. This field of inquiry also has promise for revealing novel applications of diffraction of aligned molecules. Such samples clearly add to the degrees of freedom available to the diffractionist to explore complex structures because bond angles have explicit roles in the scattering patterns, as seen in expressions such as Equation (15). It is simple with the laser-induced alignment studied here to "rotate" the sample relative to the electron beam, as done routinely in crystallography, to get different views of the same structure. Studies of reaction dynamics may also benefit from increased scrutiny of the role of anisotropy, since almost all reactions will have implications for the rotational distribution of products. Such studies of real systems will require departing from some of the idealized assumptions in the current work, but we believe that the development given here reveals many of the fundamental principles at play and establishes reference points with which future theoretical and experimental studies may be compared.

Note added in proof: Herein, explicit scattering expressions were given for two special cases, those of parallel and perpendicular laser polarization. The corresponding expression for the case of arbitrary polarization has now been obtained and will be discussed in detail, including "magic-angle" conditions, in a forthcoming publication.

Acknowledgments

This research was supported by the National Science Foundation and the Air Force Office of Scientific Research.

Keywords: femtochemistry · gas-phase reactions · molecular structures · oriented molecules · ultrafast electron diffraction

[1] *Stereochemical Applications of Gas-Phase Electron Diffraction* (Eds.: I. Hargittai, M. Hargittai), VCH, New York, 1988, and references therein.

[2] A. H. Zewail, *Phil. Trans. R. Soc. A* 2005, 364, 315–329.

- [3] R. Srinivasan, V. A. Lobastov, C.-Y. Ruan, A. H. Zewail, *Helv. Chim. Acta* **2003**, *86*, 1763–1838.
- [4] J. C. Williamson, A. H. Zewail, *J. Phys. Chem.* **1994**, *98*, 2766–2781.
- [5] A. A. Ischenko, L. Schäfer, J. D. Ewbank, *J. Mol. Struct.* **1996**, *376*, 157–171.
- [6] W.-K. Liu, S. H. Lin, *Phys. Rev. A* **1997**, *55*, 641–647.
- [7] J. S. Baskin, A. H. Zewail, *J. Phys. Chem.* **1994**, *98*, 3337–3351.
- [8] J. S. Baskin, A. H. Zewail, *J. Phys. Chem. A* **2001**, *105*, 3680–3692.
- [9] R. N. Zare, *Angular Momentum*, Wiley, New York, **1988**, p. 226.
- [10] G. Arfken, *Mathematical Methods for Physicists*, 2nd ed., Academic Press, New York, **1970**, p. 522.
- [11] P. M. Felker, A. H. Zewail in *Femtosecond Chemistry*, Vol. I (Eds.: J. Manz, L. Wöste), VCH, New York, **1994**, pp. 193–260, and references therein.
- [12] P. M. Felker, *J. Phys. Chem.* **1992**, *96*, 7844–7857.
- [13] G. Herzberg, *Molecular Spectra and Molecular Structure*, Vol. II, Van Nostrand Reinhold, New York, **1945**, p. 23.
- [14] P. M. Felker, A. H. Zewail, *J. Chem. Phys.* **1987**, *86*, 2460–2482; P. M. Felker, J. S. Baskin, A. H. Zewail, *J. Phys. Chem.* **1986**, *90*, 724–728.
- [15] M. Gruebele, A. H. Zewail, *J. Chem. Phys.* **1993**, *98*, 883–902.
- [16] V. Typke, M. Dakkouri, H. Oberhammer, *J. Mol. Struct.* **1978**, *49*, 85–96.
- [17] G. Herzberg, *Molecular Spectra and Molecular Structure*, Vol. III, Van Nostrand Reinhold, New York, **1966**, pp. 609, 621.

Received: June 23, 2005